

Particle-hole symmetry and interaction effects in the Kane-Mele-Hubbard model

Dong Zheng,^{1,2} Guang-Ming Zhang,¹ and Congjun Wu²

¹*State Key Laboratory of Low-Dimensional Quantum Physics and
Department of Physics, Tsinghua University, Beijing, China 100084*

²*Department of Physics, University of California, San Diego, CA 92093*

We prove that the Kane-Mele-Hubbard model with purely imaginary next-nearest-neighbor hoppings has a particle-hole symmetry at half-filling. Such a symmetry has interesting consequences including the absence of charge and spin currents along open edges, and the absence of the sign problem in the determinant quantum Monte-Carlo simulations. Consequentially, the interplay between band topology and strong correlations can be studied at high numeric precisions. The process that the topological band insulator evolves into the antiferromagnetic Mott insulator as increasing interaction strength is studied by calculating both the bulk and edge electronic properties. In agreement with previous theory analyses, the numeric simulations show that the Kane-Mele-Hubbard model exhibits three phases as increasing correlation effects: the topological band insulating phase with stable helical edges, the bulk paramagnetic phase with unstable edges, and the bulk antiferromagnetic phase.

PACS numbers: 05.50.+q, 71.30.+h, 73.43.-f, 73.43.Nq

I. INTRODUCTION

The precise quantization of the Hall conductance in the integer quantum Hall states is protected by the non-trivial topology of band structures. This topological property is characterized by the Thouless-Kohmoto-Nightingale-den Nijs (TKNN) number, or the Chern number [1, 2], which takes non-zero values only when time-reversal symmetry is broken. In recent years, tremendous progress has been achieved in a new class of topologically non-trivial band insulators in the presence of time-reversal symmetry, which are termed as topological insulators [3–13]. Topological insulators exist in both two (2D) and three dimensions (3D), which are characterized by the Z_2 topological index. These topological states have robust gapless helical edge modes with odd number of channels in 2D [7, 14, 15], and odd number of surface Dirac cones in 3D [11–13]. Topological insulators have been experimentally observed in 2D quantum wells through transport measurements [16], and also in 3D systems of $\text{Bi}_x\text{Sb}_{1-x}$, Bi_2Te_3 , Bi_2Se_3 , and Sb_2Te_3 through the angle-resolved photo-emission spectroscopy [17–20], and the absence of backscattering in the scanning tunneling spectroscopy [21–23].

Interaction effects in topological insulators remain an open question. Due to their gapped nature, topological insulators remain stable against weak interactions. However, strong interactions may change their topological properties. For 2D topological insulators, it has been found that the two-particle correlated backscattering, which is an interaction effect and is allowed in the time-reversal invariant Hamiltonian, can gap out the helical edge states by spontaneously developing magnetic ordering under strong repulsive interactions [14, 15]. In this case, time-reversal symmetry is spontaneously broken along edges, although the bulk remains paramagnetic. At mean-field level, interaction effects can destabilize the quantum anomalous Hall state of the Haldane-

Hubbard model [24] and the 2D topological insulating state of the Kane-Mele-Hubbard (KMH) model [25] by developing long-range charge density wave and antiferromagnetic orders, respectively [25]. Interactions can also change the topologically trivial band structures into non-trivial ones at mean-field level by developing bulk order parameters [26–29]. Due to the difficulty of analytic studies on strong correlation physics, exact results from numeric simulations are desirable. Recently, an exact diagonalization has been carried on the spinless Haldane-Hubbard model [30]. A first order phase transition between quantum anomalous Hall insulating state and topologically trivial Mott-insulating state is found.

Quantum Monte-Carlo (QMC) simulations play an important role in studying strongly correlated systems [31–34]. A major obstacle to apply the QMC to fermion systems is the notorious sign problem. In the particular method of the determinant QMC, the 4-fermion interaction terms are decoupled through the Hubbard-Stratonovich (HS) transformation and fermions are able to be integrated out. The resultant fermion determinant, generally speaking, is not positive-definite, which is the origin of the notorious sign problem. This problem prevents QMC simulations to achieve a good numerical precision at low temperatures and large sample sizes. Nevertheless, in a number of interacting models, the sign problem disappears. As presented in Ref. [35], these models include the negative- U Hubbard model, the positive- U Hubbard model at half-filling and in bipartite lattices, and a class of models whose interactions can be decomposed in a time-reversal invariant way.

We find that the Kane-Mele model augmented by the Hubbard interaction with purely imaginary next-nearest-neighbor hoppings has a particle-hole symmetry. Such a symmetry has interesting consequences such as the absence of edge charge and spin currents, which shows the edge currents are not a reliable criterion for topological properties. More importantly, the particle-hole symme-

try ensures the absence of the sign problem in the quantum Monte-Carlo simulations. This provides a wonderful opportunity to study interaction effects in topological insulating systems.

In this article, we perform a determinant QMC study on the stability of the topological insulating state of the KMH model with the strong Hubbard interaction U . Antiferromagnetic long-range-order has been found at large values of U . Consequently, the quantum phase diagram of the KMH model can be classified into paramagnetic bulk insulating phases and antiferromagnetic Mott insulating phases. When further consider the stability of helical edges with infinitesimal two-particle backscattering, which is not contained in KMH model but generally allowed by time-reversal symmetry, the paramagnetic bulk insulating phase can be divided into two regimes according to their edge state Luttinger parameters [14]. The topological band insulator with stable helical edges are stable in the weak interaction regime, while the helical edges become unstable by two-particle correlated backscattering at the intermediate interaction regime. We have also studied the nature of spin-liquid phase in the pure Hubbard model with $\lambda = 0$, showing that it is neither a spontaneous Haldane type quantum anomalous Hall insulator, nor, a Kane-Mele type quantum spin Hall insulator.

This article is organized as follows. In Section II, we prove the absence of the sign problem in the KMH model under certain conditions. In Section III, we present the simulations on the developing of antiferromagnetic long-range orders in the bulk. In Section IV, the edge properties are studied including both the edge single particle excitations and the edge spin correlations. In Section V, we present the simulation of the charge and spin current orders in the pure Hubbard model in the honeycomb lattice. Conclusions are given in Section VI.

II. GENERAL PROPERTIES OF THE KMH MODEL

The Kane-Mele model is a straightforward generalization of the Haldane model in the honeycomb lattice [7] defined as

$$H_0 = -t \sum_{\langle i,j \rangle, \sigma} c_{i\sigma}^\dagger c_{j\sigma} + i\lambda \sum_{\langle\langle i,i' \rangle\rangle, \alpha, \beta} \left\{ c_{i\alpha}^\dagger \sigma_{z, \alpha\beta} c_{i'\beta} - c_{i'\alpha}^\dagger \sigma_{z, \alpha\beta} c_{i\beta} \right\} - \mu \sum_{i, \sigma} c_{i\sigma}^\dagger c_{i\sigma}, \quad (1)$$

where t is the nearest-neighbor (NN) hopping integral as scaled to 1 below; λ is the next-nearest-neighbor (NNN) spin-orbit hopping integral; μ is the chemical potential. In the general case of the Kane-Mele model, the NNN hopping for the spin- \uparrow (\downarrow) electrons are complex-valued and complex-conjugate to each other. As a special case, the NNN hopping in Eq. 1 is purely imaginary. The

Hubbard interaction is defined as usual

$$H_{int} = U \sum_i \left[n_{i\uparrow} - \frac{1}{2} \right] \left[n_{i\downarrow} - \frac{1}{2} \right]. \quad (2)$$

In this section, we will present the symmetry properties of Eq. 1 and Eq. 2, and prove the absence of the sign problem in the determinant QMC.

A. Particle-hole symmetry

Eq. 1 and Eq. 2 has the particle-hole symmetry at $\mu = 0$ as explained below. We define the transformation as usual

$$c_{i\sigma}^\dagger \longrightarrow d_{i\sigma} = (-1)^i c_{i\sigma}^\dagger, \quad c_{i\sigma} \longrightarrow d_{i\sigma}^\dagger = (-1)^i c_{i\sigma}. \quad (3)$$

Under this transformation, a Hermitian fermion bilinear operator connecting two sites belonging to two different sublattices transforms as

$$c_{i\sigma}^\dagger K_{ij} c_{j\sigma} + c_{j\sigma}^\dagger (K_{ij})^* c_{i\sigma} \longrightarrow d_{i\sigma}^\dagger (K_{ij})^* d_{j\sigma} + d_{j\sigma}^\dagger K_{ij} d_{i\sigma}, \quad (4)$$

while that connecting two different sites in the same sublattice transforms as

$$c_{i\sigma}^\dagger K_{ii'} c_{i'\sigma} + c_{i'\sigma}^\dagger (K_{ii'})^* c_{i\sigma} \longrightarrow -d_{i\sigma}^\dagger (K_{ii'})^* d_{i'\sigma} - d_{i'\sigma}^\dagger K_{ii'} d_{i\sigma}. \quad (5)$$

The onsite particle density transforms as

$$c_{i\sigma}^\dagger c_{i\sigma} - \frac{1}{2} \longrightarrow \frac{1}{2} - d_{i\sigma}^\dagger d_{i\sigma}, \quad (6)$$

where no summation over spin-index is assumed in Eq. 6. Clearly in Eq. 1, the NN-hopping is real and the NNN-hopping is purely imaginary, thus its band structure is invariant at $\mu = 0$. Eq. 2 is obviously invariant. The particle-hole symmetry also implies that $\mu = 0$ corresponds to half-filling.

B. Absence of the charge and spin currents

An important conclusion based on the particle-hole symmetry is that both charge and spin currents vanish on all the bonds for the KMH model of Eq. 1 and Eq. 2 at $\mu = 0$. This result applies to arbitrary boundary conditions with broken bonds but with the homogeneous onsite potential which maintains the particle-hole symmetry on each site. The proof is straightforward. Through the continuity equation, the current operators of each spin component along the NN and NNN bonds are defined as

$$J_{ij, \sigma}^{NN} = it(c_{i\sigma}^\dagger c_{j\sigma} - c_{j\sigma}^\dagger c_{i\sigma}), \quad J_{ii', \sigma}^{NNN} = \lambda(c_{i\sigma}^\dagger c_{i'\sigma} + c_{i'\sigma}^\dagger c_{i\sigma}), \quad (7)$$

respectively, where no summation over spin-index is assumed. Both J^{NN} and J^{NNN} are odd under the particle-hole transformation, thus they vanish even with the open-boundary condition. By the same reasoning, the charge current also vanishes in the Haldane-Hubbard model with the purely imaginary NNN-hoppings and the particle-hole symmetric charge interactions of

$$H_{NN,int} = \sum_{ij} V_{ij} (n_i - \frac{1}{2})(n_j - \frac{1}{2}). \quad (8)$$

This result shows that edge charge and spin currents are not good criteria for quantum anomalous Hall and topological insulators. In order to have a better understanding on this counter-intuitive result, we have considered the simplest non-interacting Haldane model with the purely imaginary NNN hoppings by diagonalization. There are indeed gapless one-dimensional single particle chiral edge modes clearly seen from the spectra as commonly presented in literatures. Clearly this branch of edge mode contributes to edge currents. However, we find that the continuous bulk spectra also contribute to edge currents. Perfect cancellation occurs which results in zero current on each bond, including each edge bond, although we know for sure that the band structure is topologically non-trivial. For interacting models, there are no well-defined single particle states. We cannot separate the edge and bulk contributions anymore. Nevertheless, we expect that current correlation functions should exhibit difference between topological insulators and trivial insulators.

Another conclusion inferred from the particle-hole symmetry is that the average particle density for each spin component on each site is strictly $\frac{1}{2}$ even when the translational symmetry is broken. For example, it applies to any disordered pattern of the hopping integrals, as long as the NN hoppings are real and the NNN hoppings are purely imaginary.

Edge currents do appear if the particle-hole symmetry is broken. For example, for the non-interacting Haldane model with generally complex-valued NNN hoppings, edge currents appear along open boundaries. So far we only consider the sharp edges of broken bonds but with homogeneous on-site potential. For edges with the confining single particle potential, the particle-hole sym-

metry is broken which also results in edge currents. In particular, for a weak linear external potential, the linear response should still give rise to quantized Hall conductance in the insulating region.

C. Absence of the QMC sign problem

The Hubbard model on the honeycomb lattice, which corresponding to the case of $\lambda = 0$ of Eq. 1 and Eq. 2 has been recently simulated at half-filling [36]. As Hubbard U increases from zero to a moderate value and then the strong coupling regime, the ground state emerges from a semi-metal phase, to a new spin-liquid phase and then the antiferromagnetic insulating phase. Below we will prove that the sign problem still vanishes with nonzero values of λ . The absence of the sign problem can be proved for both the finite temperature and the zero temperature algorithms for the determinant QMC. In this subsection, we prove this property for the finite temperature method for simplicity, and leave the more lengthy proof for the zero temperature algorithm in Appendix A. We emphasize that the simulations presented in this article are done at the zero temperature.

Just as the Ref.([36]) does, we employ a discrete HS transformation which respects the $SU(2)$ symmetry for every fixed HS field configuration by decoupling in the density channel. We rewrite the Hubbard interaction and decompose it in the density channel by using imaginary numbers as

$$e^{-\Delta U(n_{\uparrow}+n_{\downarrow}-1)^2/2} = \sum_{l=\pm 1, \pm 2} \gamma_i(l) e^{in_i(l)\sqrt{\Delta\tau U/2}(n_{\uparrow}+n_{\downarrow}-1)} + \mathcal{O}(\Delta\tau^4). \quad (9)$$

where the discretized HS fields take values of $\gamma(\pm 1) = 1 + \sqrt{6}/3$, $\gamma(\pm 2) = 1 - \sqrt{6}/3$; $\eta(\pm 1) = \pm\sqrt{2(3-\sqrt{6})}$, and $\eta(\pm 2) = \pm\sqrt{2(3+\sqrt{6})}$.

For the convenience of presentation, we prove the absence of the sign problem in the finite temperature formalism with $\beta = 1/T$. The proof for the zero temperature projector algorithm is similar. The partition function at half-filling reads

$$Z = \sum_{\{l\}} \left\{ \left(Tr \prod_{p=M}^1 e^{-\Delta\tau \sum_{i,j} c_{i\uparrow}^\dagger K_{ij}^\uparrow c_{j\uparrow}} e^{i\sqrt{\Delta\tau U/2} \sum_i \eta_{i,p}(l) (c_{i\uparrow}^\dagger c_{i\uparrow} - \frac{1}{2})} \right) \times \left(Tr \prod_{p=M}^1 e^{-\Delta\tau \sum_{i,j} c_{i\downarrow}^\dagger K_{ij}^\downarrow c_{j\downarrow}} e^{i\sqrt{\Delta\tau U/2} \sum_i \eta_{i,p}(l) (c_{i\downarrow}^\dagger c_{i\downarrow} - \frac{1}{2})} \right) \prod_{i,p} \gamma_{i,p}(l) \right\}, \quad (10)$$

where $\sum_{\{l\}}$ sums over all the configurations of the dis-

crete HS fields $\eta_{i,p}(l)$ and $\gamma_{i,p}(l)$; i and p are indices of dis-

cretized grids along the spatial and temporal directions, respectively; Tr takes the trace of the fermion space; $\Delta\tau$ is the discretized time slice which is set to 0.05 in the simulations in this article; $M\Delta\tau$ equals the imaginary time β . By using the particle-hole transformation defined in Eq. 3, we show that the onsite particle density transforms according to Eq. 6; the NN-hopping matrix kernel transforms according to Eq. 4; the NNN-hopping matrix kernel transforms according to Eq. 5.

When the following two conditions are satisfied, the fermion determinants of two spin components are complex-conjugate to each other, thus the product of them is positive-definite:

$$\begin{aligned} K_{ij}^\sigma &= (K_{ji}^{\bar{\sigma}})^* = K_{ij}^{\bar{\sigma}} \quad \text{for NN-hopping;} \\ K_{ij}^\sigma &= -(K_{ji}^{\bar{\sigma}})^* = -K_{ij}^{\bar{\sigma}} \quad \text{for NNN-hopping.} \end{aligned} \quad (11)$$

Apparently, Eq. 1 and Eq. 2 satisfy these conditions, and thus are sign problem free.

Please note that the KMH mode is sign problem free only when the NNN-hopping is purely imaginary. Generally speaking, the interacting model without the sign problem can have complex-valued hoppings with opposite signs, which still gives rise to opposite Chern numbers for the band structures of spin- \uparrow and \downarrow , respectively. However, they are not related by time-reversal symmetry anymore.

III. THE QMC STUDY ON THE BULK PROPERTIES OF THE KMH-MODEL

The Hubbard model in the honeycomb lattice, which corresponds the case of $\lambda = 0$ in Eq. 1 and Eq. 2, has been simulated in Ref. [36]. When U increases from zero, the single particle charge gap appears at $U = 3.7$, while the antiferromagnetic long-range order emerges at $U = 4.3$. The mismatch reveals an exotic spin liquid phase in between. When the intrinsic spin-orbit coupling, *i.e.*, the NNN hopping term in Eq. 1, enters, the model describes the topological band insulator. It already has a band gap even at $U = 0$. As increasing U , the antiferromagnetic structure factor is still a good quantity to tell when the magnetic long range order appears. However, the bulk gap is no longer an appropriate quantity to judge a possible transition from the topological band insulator to an antiferromagnetic Mott-insulator. Here we use the local single particle gap on edge sites as an indicator of the stability of edge states and topological properties. We also study the edge effects to antiferromagnetic correlations. In this section, we will simulate the bulk antiferromagnetic structure factor, and leave the study of edge properties in Section IV.

A. Sampling parameters of our simulations

Based on the above proof of the absence of the sign problem, we perform the QMC simulation for the KMH

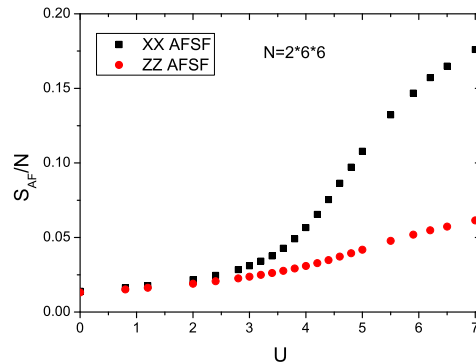


FIG. 1: (Color online) The comparison between the antiferromagnetic structure factors S_{AF}^{zz} along the z -axis and S_{AF}^{xx} in the xy -plane at $\lambda = 0.1$ for the size of $N = 2 \times L \times L$ with $L = 6$. The easy-plane feature is clear.

model at *zero temperature* by using the projective method [37]. We perform measurements from 10 different random number series and each independent measurement has 500 sample sweeps after warming up, the discrete imaginary time step $\Delta\tau$ is set to be 0.05. In this section, we use periodic boundary conditions for bulk properties calculation, *e.g.*, the bulk antiferromagnetic structure factor.

B. The developing of the bulk antiferromagnetic long range order

The spin-orbit NNN hopping in Eq. 1 breaks the $SU(2)$ symmetry but preserves the conservation of S_z . As a result, the antiferromagnetic correlation of S_z should be different from those of S_x and S_y . In the large U -limit, the NNN hopping generates an anisotropic exchange as

$$H_{ex,NNN} = -J' (S_i^x S_{i'}^x + S_i^y S_{i'}^y - S_i^z S_{i'}^z) \quad (12)$$

with $J' = 4\lambda^2/U$, which is ferromagnetic in the xy -plane and antiferromagnetic along the z -direction [25]. As the combined effect from the NNN anisotropic exchange and NN isotropic antiferromagnetic exchange, the magnetic exchange along the z -axis is frustrated while those along x and y -axes are not. Thus the Neel ordering favors the easy xy -plane.

Our QMC simulations have confirmed this picture. The antiferromagnetic structure factor along the x -direction (xx -AFSF) and the z -direction (zz -AFSF) are defined as

$$\begin{aligned} S_{AF}^{xx} &= \frac{1}{N} \langle G | \left[\sum_i (-1)^i S_i^x \right]^2 | G \rangle, \\ S_{AF}^{zz} &= \frac{1}{N} \langle G | \left[\sum_i (-1)^i S_i^z \right]^2 | G \rangle, \end{aligned} \quad (13)$$

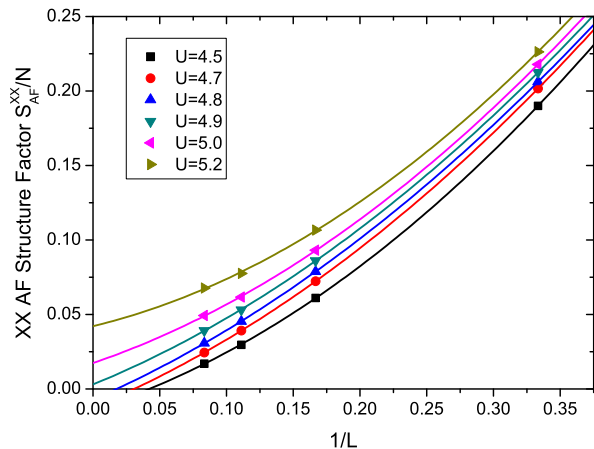


FIG. 2: (Color online) The finite-size scaling of the xx -antiferromagnetic structure factors calculated at $\lambda = 0.1$ for the sizes of $N = 2 \times L \times L$ ($L = 3, 6, 9$ and 12), and the different values of U indicated in the inset. Finite values of S_{AF}^{xx}/N in the thermodynamic limit appear at $U \geq U_c$ with $U_c \approx 4.9$.

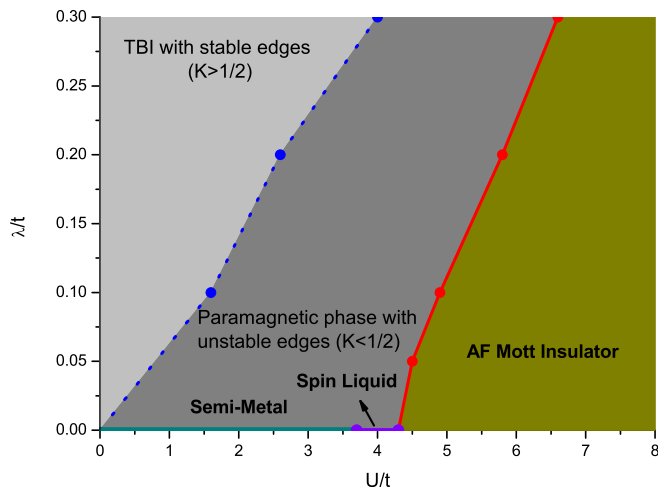


FIG. 3: (Color online) The QMC simulation of the phase diagram of the KMH model. The antiferromagnetically long-range ordered phase appears at strong correlation regime. The paramagnetic phase is divided into two regimes: topological band insulator (TBI) with stable helical edges, and bulk paramagnetic phase with unstable edges (see further discussions in Sect. IV C). The two critical values of U at $\lambda = 0$ are from Ref. [36] by Meng *et al.*, which are also confirmed in our QMC simulations.

where $\langle G | \dots | G \rangle$ means average over the ground state; $N = 2 \times L \times L$ is the number of sites; L is the size; $(-)^i$ takes the values of ± 1 for the A and B -sublattices, respectively. The comparison between S_{AF}^{xx} and S_{AF}^{yy} is plotted in Fig. 1, which clearly shows the easy-plane feature.

Below we will use the xx -AFSF to describe the anti-ferromagnetic properties, and perform the simulation at $\lambda = 0.1$ with different values of U and sample sizes of $L = 3, 6, 9, 12$. The extrapolation to the thermodynamic

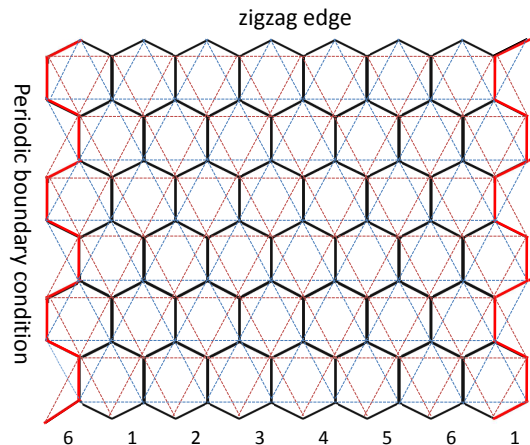


FIG. 4: (Color online) The KMH model in the lattice with the zig-zag edges. The boundary conditions are periodical and open along the x and y -directions, respectively. The NNN-bonds between two closest tips on the zig-zag edges are removed.

limit for different Hubbard U is plotted in of Fig. 2. It can be seen that the magnetic long range order emerges at $U_c = 4.9 \pm 0.1$ for $\lambda = 0.1$. In Fig. 3 we present the QMC simulation on the magnetic phase diagram of the KMH model for in the parameter space of (U, λ) . The phase boundary separating the AF long-range-ordered phase and non-magnetic phases are marked for various values of λ . The spin-orbit coupling opens the band gap at the order of λ , thus the interaction effect U becomes important only when U is larger than λ . As a result, the critical value of U_c for the onset of the AF phase increases with λ .

The phase diagram Fig. 3 exhibits a large regime of non-magnetic insulating state outside the AF phase at $\lambda \neq 0$. At small values of U , it should be the Z_2 topological band insulating phase which is stable against weak interactions. As increasing U , it enters the AF Mott insulating phase at a critical line of U_c . In an updated version of Ref. [40], it is found that the spin-liquid phase also extends to a small but finite value of λ . However, the nature of this spin-liquid state remains unclear. The bulk paramagnetic regime actually has rich internal structures. According to the stability of the helical edge states with respect to the two-particle spin-flip backscattering, this paramagnetic insulating phase is divided into two different regimes with the effective edge Luttinger parameter $K < (>) \frac{1}{2}$, respectively. The analysis is presented below in Sect. IV C.

IV. THE QMC STUDY OF THE EDGE PROPERTIES OF THE KMH MODEL

We believe that the edge properties is crucial to expose the topological aspect of the KMH model. In this section, we will show that the antiferromagnetic correlations

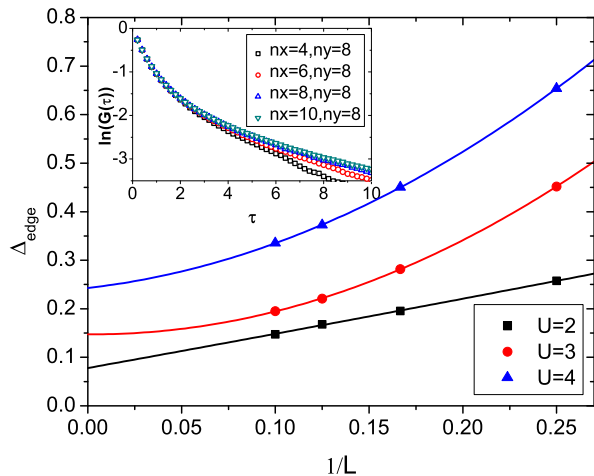


FIG. 5: (Color online) The extrapolation of local single particle gap for the tip sites on the zig-zag edges of a ribbon geometry with the size of $2 \times L \times n_y$ with $n_y = 8$. In the inset, the logarithms of onsite time-displaced Green's functions $\ln G(i, i; \tau)$ of the tip sites is depicted for $U = 2$. The slopes of the long time tails measure the edge excitation gap Δ_{edge} . Here λ is set to be 0.1 in this calculation. Due to the one-dimensional nature of the edge, its densities of states in the thermodynamic limit are depleted according to the power-law determined by the Luttinger parameter, and thus are difficult to be distinguished from finite gaps.

along the edge become strongly relevant as increasing the Hubbard U while the bulk remains paramagnetic. We consider the lattice configuration plotted in Fig. 4 with the periodical and open boundary conditions along the x and y -directions, respectively.

A. The single-particle excitations

As proved in Sect. II, the edge currents, both for charge and spin, are always zero due to the particle-hole symmetry. We use another quantity, the local single particle excitation gap on edge sites, to check whether the edges are gapped or gapless. It can be extracted from the tail of on-site time displaced Green's function on the edge $\ln G(i, i; \tau) \sim \Delta_{edge} \tau$, which is defined by

$$G(i, i; \tau) = \frac{1}{L} \langle G | \sum_{i \in \text{tip}} c_{i\uparrow}^\dagger(\tau) c_{i\uparrow}(0) + c_{i\downarrow}^\dagger(\tau) c_{i\downarrow}(0) | G \rangle, \quad (14)$$

where $|G\rangle$ is the many-body ground state. The dependency of $\ln G(i, i; \tau)$ with τ for the site i on the tip of the zig-zag edges are plotted in the inset of Fig. 5, where the long tail of $\ln G(i, i; \tau)$ shows a linear behavior with τ and the slope measures the excitation gap. Here the lattice has a ribbon geometry with n_y zig-zag rows. We fix the width of the ribbon $n_y = 8$ and increase its length. The extrapolations of the edge excitation gaps with L are depicted in Fig. 5 with λ fixed at 0.1 and different values

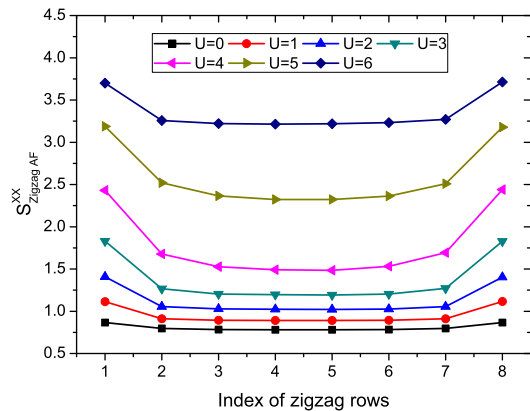


FIG. 6: (Color online) The row xx -AFSF defined in Eq. 16 for each zig-zag rows parallel to the boundary. The parameters values are $\lambda = 0.1$; the sample size $2 \times L \times L$ with $L = 8$; and different values of U indicated in the inset. The row-indices 1 and 8 correspond to the boundary rows, and those of 4 and 5 corresponds to the central rows.

of $U < U_c$. Clearly increasing U significantly reduces the weight of the low energy spectra.

The bosonization analysis of the stability of the helical edge states has been performed in Ref. [14, 15]. For the parameter regime of Fig. 5, the bulk remains paramagnetic, or, time-reversal invariant. For the current KMH-model, S_z is conserved which prohibits the existence of the two-particle spin-flip scattering term to open the gap. The Luttinger liquid theory of such a helical edge branch, *i.e.*, the right and left movers are with opposite spin polarizations, is characterized by only one Luttinger parameter K , which describes the forward scattering between these two branches. Due to the helical nature of the edge states, the long wavelength charge fluctuations and the z -component of the spin fluctuations are not independent but are conjugate to each other. Both of them are gapless in the thermodynamic limit, and so does the single particle edge excitations. The onsite imaginary time single-particle Green's function decays as $1/\tau^\alpha$ with the exponent

$$\alpha = K + 1/K. \quad (15)$$

At $K \ll 1$, the low energy density of states does not open a full gap but are depleted according to a power-law, and thus exhibit a pseudo-gap behavior. The non-zero gap values in Fig. 5 may be an artifact of finite size scaling and a result of tunneling between two opposite edges. A more detailed numerical analysis is needed to further clarify the nature of the single particle excitations.

B. Edge spin structure factors

We further investigate the edge effects to the antiferromagnetic correlations. We define the antiferromagnetic structure form factor for each zig-zag row parallel to the

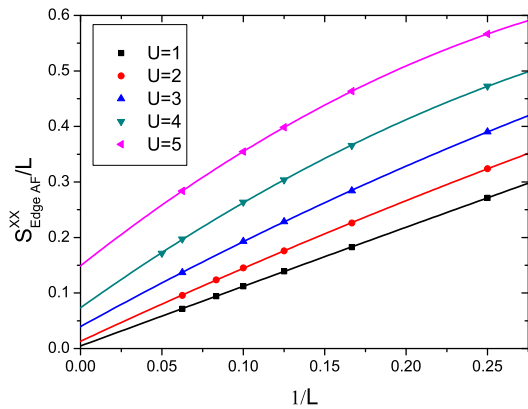


FIG. 7: (Color online) The finite size scaling of the xx -AFSF defined in Eq. 16 for the edge row with $\lambda = 0.1$. The size of this ribbon is $2 \times L \times 4$. We emphasize that due to the 1D nature of the edge and the $U(1)$ spin symmetry, this scaling actually shows the power-law correlation rather than the true-long-range order. The finite intercepts are mainly due to small size effects.

zig-zag boundary as

$$S_{Zigzag,AF}^{xx}(m) = \frac{1}{2L} \langle G | [\sum_i (-1)^i S_{m,i}^x]^2 | G \rangle, \quad (16)$$

where m is the index of the zig-zag row; i is the site index along the m -th zig-zag line; $2L$ is the number of sites in each row. The xx -AFSF for all the rows are depicted in Fig. 6.

It is interesting to observe that the AF correlations are strongest on edges, and become weaker inside the bulk. This effect is most prominent at small and intermediate values of U , because the single particle band gap due to λ is suppressed around edges, which enhances the interaction effects. When $U \geq U_c \approx 4.9$, the bulk antiferromagnetism develops. The antiferromagnetic correlations along both the edge and central rows are enhanced by U . However, their difference is suppressed due to the disappearance of the helical edge states.

The finite-size scaling of the xx -AFSF for the edge rows for different values of U are presented in Fig. 7. Compared with the xx -AFSF calculated in the bulk (Fig. 2), the edge antiferromagnetic correlations are much stronger than those of the bulk. Although the extrapolation to the infinite size in Fig. 7 implies a finite value of the Neel order of S_x on the edge, we believe that it is an artifact due to the power-law scaling of the AF correlations. The 1D nature of the edge states and the conservation of S_z prohibits the true long range Neel ordering of $S_{x,y}$ but allows the quasi-long-range ordering, which is confirmed in the two-point spin correlations in Sect. IV C.

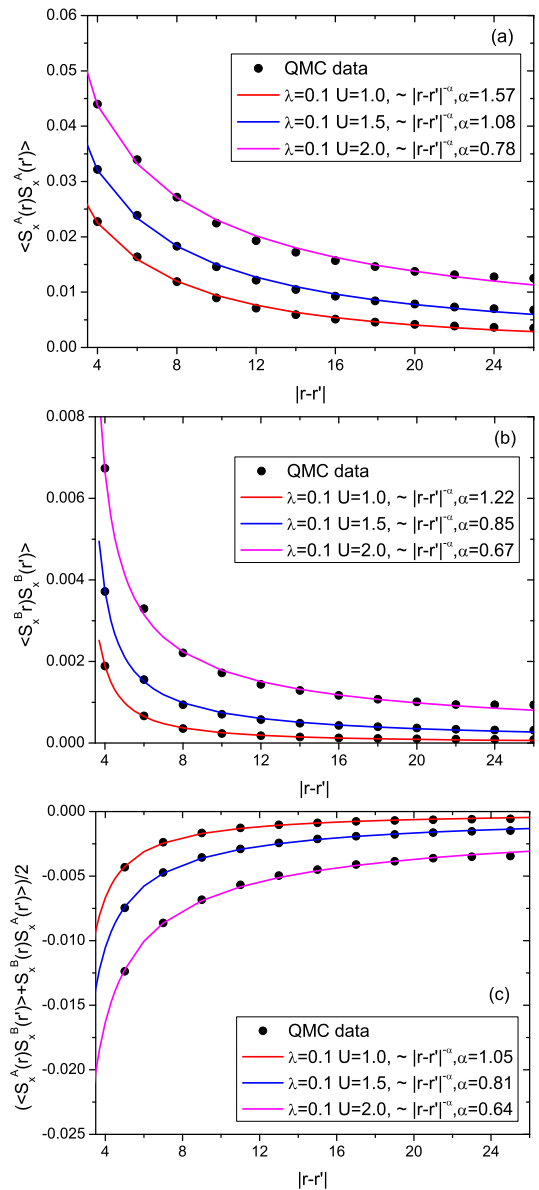


FIG. 8: (Color online) The two-point equal-time spin correlation functions along the zig-zag edge with $\lambda = 0.1$ at values of U denoted in the insets. The sizes of the ribbon is $2 \times 34 \times 4$. Because the zig-zag edge contains the sites of both A and B type, three different types of correlations are plotted in (a), (b), and (c), respectively. The Luttinger parameters are fitted from the correlation among A -sites on the tips as $K \approx 0.8, 0.5$ and 0.4 for $U = 1, 1.5$ and 2 , respectively.

C. The stability of the helical edges

According to the bosonization analysis in Ref. [14], the scaling dimension of the $2k_f$ Neel order of the xy -components is K , thus their equal-time correlations decays as $1/|x - x'|^{2K}$. If the condition of the conservation of S_z is released, a time-reversal invariant two-particle

correlated spin-flip backscattering term is allowed as

$$H_{bg,2pct} = \int dx \psi_{R\uparrow}^\dagger \partial_x \psi_{R\uparrow} \psi_{L\downarrow}^\dagger \partial_x \psi_{L\downarrow} + h.c. \quad (17)$$

At the particle-hole symmetric point of the KMH-model that we are simulating, the above term becomes the Umklapp term which conserves the lattice momentum. Such a term reduces the $U(1)$ spin symmetry down to Z_2 . It has the scaling dimension $4K$, and becomes relevant at $K < K_c = 1/2$. In this case, it opens a gap by developing the long range $2k_f$ magnetic ordering of S_x or S_y . Even for the cases that the two-particle spin-flip backscattering are random disordered or at a single site, they still can destabilize the helical edge states at smaller values of the Luttinger parameter K [14].

According to the above analysis, the bulk paramagnetic regime at weak and intermediate coupling strengths should be divided into two regimes. At weak interactions, the helical edge states are stable against interaction effects. The two-particle backscattering terms only have perturbative effects. On the other hand, at intermediate level of interaction strength, interaction effects are non-perturbative which breaks time-reversal symmetry along edges and thus destroys the helical edges. We emphasize that this destabilizing helical edges occurs when the bulk remains paramagnetic and time-reversal invariant.

To numerically verify this picture, we present the calculation of the real space equal-time two-point correlations along the zig-zag edge in Fig. 8. Since each unit cell contains two non-equivalent sites, we denote the sites on the tips of the edge as A -sites and the other slightly inner sites as B -sites. The correlation functions are defined as

$$\begin{aligned} C_{AA}(r, r') &= \langle G | S_x^A(\vec{r}) S_x^A(\vec{r}') | G \rangle, \\ C_{BB}(r, r') &= \langle G | S_x^B(\vec{r}) S_x^B(\vec{r}') | G \rangle, \\ C_{AB}(r, r') &= \frac{1}{2} \{ \langle G | S_x^A(\vec{r}) S_x^B(\vec{r}') | G \rangle \\ &\quad + \langle G | S_x^B(\vec{r}) S_x^A(\vec{r}') | G \rangle \}, \end{aligned} \quad (18)$$

where \vec{r} and \vec{r}' are along the zig-zag edge. The simulated results for $\lambda = 0.1$ are plotted at different values of U in the bulk paramagnetic regime. The edge spin correlation exhibits the ferrimagnetic correlations among A and B -sites because the edge breaks the equivalence between A and B -sites. The magnetic correlations are stronger among the outer A -sites, and are weaker among the inner B -sites. All of these correlations obey the power law and their decay exponents (α) are fitted. As further increasing U towards to the bulk antiferromagnetic regime, the difference between AA and BB correlations become weaker.

Due to the domination of the magnetic correlation at A -sites, we use the decay exponents of C_{AA} to fit the effective Luttinger parameter K for the helical edge. The three plots in Fig. 8 (a) at $U = 1, 1.5$ and 2 gives rises to $K = \frac{1}{2}\alpha \approx 0.8, 0.5$, and 0.4 , respectively. The case of $U = 1$ belongs to the topological band insulating phase in

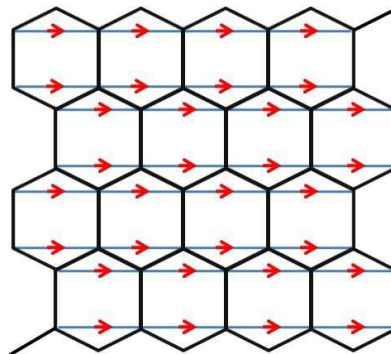


FIG. 9: (Color online) The definition of the positive direction for the NNN bonds in the honeycomb lattice, based on which the NNN current form factors Q_C^{AF} and Q_S^{AF} are defined in Eq. 19.

which interaction effects are perturbative. For the case of $U = 2$ at which the bulk remains non-magnetic, although the edge remains gapless, it is only because the conservation of S_z which is *not* an essential symmetry of topological insulators. As long as the above Umklapp term Eq. 17 is introduced, which unfortunately cannot be simulated by our QMC method, the gapless helical edge states are destabilized. We argue that the system enters a new phase with paramagnetic bulk but unstable edges. The transition point between these two paramagnetic phases at $\lambda = 0.1$ lies at $U \approx 1.5$ with $K \approx 0.5$.

We have calculated the edge spin correlations for other values of spin-orbit coupling and interaction parameters to map the boundary with $K = 0.5$ between two different bulk paramagnetic phases. The boundary is plotted in Fig. 3. As λ decreases, the dispersion of the edge spectra becomes more flat, and interaction effects go stronger. As a result, the boundary shifts to lower values of U . In particular at $\lambda = 0$, the edge spectra become exactly flat, we expect edge ferromagnetism at infinitesimal U due to the density of state divergence. Thus the boundary should pass the origin. In particular, the edge ferromagnetism of graphene ribbon has been simulated in Ref. [38].

V. ABSENCE OF THE SPIN-ORBIT ORDER IN SPIN LIQUID PHASE AT $\lambda = 0$

Since Meng *et al.* [36] claimed the existence of a spin-liquid phase for Hubbard model ($\lambda/t = 0$) at $3.7 < U/t < 4.3$ (see Fig. 3), it has attracted considerable interests and debates on the nature of this phase. One possibility of such a phase is that it could be a relative spin-orbit symmetry breaking phase with a non-trivial mean-field band structure [39]. If it is the case, a finite λ/t behaves like an external field to pin down the order parameter along the external spin-orbit configuration. Then the semi-metal and spin-liquid phase are indistinguishable at finite λ/t . In this section, we will check the form factor of the such a spin-orbit order parameter between NNN

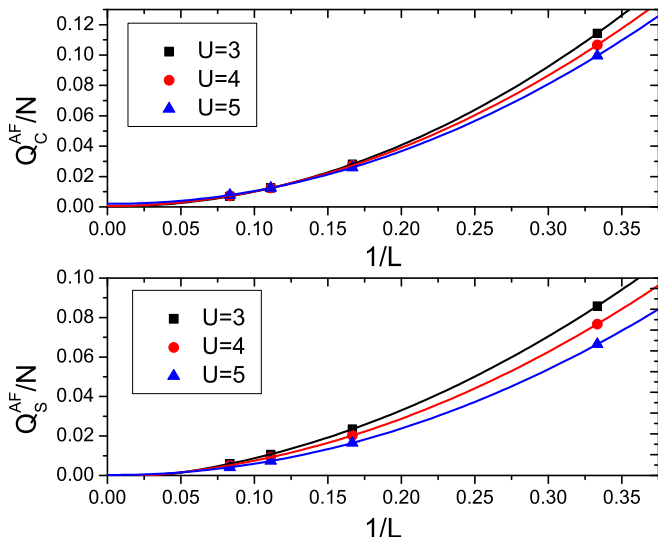


FIG. 10: (Color online) The finite-size scaling of the form factors of the NNN currents in the charge sector Q_C^{AF} and Q_S^{AF} in the spin sector as defined in Eq. 19. The periodical boundary condition is employed. The sample size is $N = 2 \times L \times L$ with $L = 3, 6, 9$ and 12 . λ is set 0 in this calculation, and $U=3, 4$ and 5 .

sites at $\lambda = 0$, and find negative results.

Without loss of generality, we only consider the horizontal bonds. We define the positive directions for the NNN horizontal bonds as depicted in Fig. 9. Two different NNN current orders are designed, including the charge flux order and the Kane-Mele type spin-orbit order, or, equivalently, the spin-current flux order. Their form factors are denoted as Q_C^{AF} and Q_S^{AF} and are defined as

$$Q_C^{AF} = \frac{1}{N} \langle G | \left\{ \sum_i (-1)^i J_{i,i+\vec{e}_x}^C \right\}^2 | G \rangle,$$

$$Q_S^{AF} = \frac{1}{N} \langle G | \left\{ \sum_i (-1)^i J_{i,i+\vec{e}_x}^S \right\}^2 | G \rangle \quad (19)$$

where $(-1)^i$ takes the values of 1 or -1 for site i in the A and B sublattices, respectively; the charge current $J_{i,i+\vec{e}_x}^C = J_{i,i+\vec{e}_x;\uparrow}^{NNN} + J_{i,i+\vec{e}_x;\downarrow}^{NNN}$, and spin current $J_{i,i+\vec{e}_x}^S = J_{i,i+\vec{e}_x;\uparrow}^{NNN} - J_{i,i+\vec{e}_x;\downarrow}^{NNN}$; \vec{e}_x is the NNN vector along horizontal direction. Please note that the bond current operator here $J_{i,i+\vec{e}_x;\sigma}^{NNN}$ is different from that in Eq. 7 as

$$J_{i,i+\vec{e}_x;\sigma}^{NNN} = i \{ c_{i,\sigma}^\dagger c_{i+\vec{e}_x,\sigma} - h.c. \}, \quad (20)$$

where no summation over σ is assumed.

We have performed the simulation of the NNN charge and spin-current form factors defined in Eq. 19 for the Hubbard model at $\lambda = 0$. The extrapolations of the form factors to the infinite lattice size are depicted in Fig. 10. The curves represents three typical Hubbard U values $U = 3, 4$ and 5 , which fall in semi-metal phase, spin-liquid phase and Mott insulating phase, respectively.

For all the three parameters, both the charge and spin NNN current antiferromagnetic form factors vanish in thermodynamic limit, indicating the absence of the NNN charge and spin-current orders in all these three phases, especially the spin liquid phase. The nature of this spin-liquid phase, whether it is actually a subtly ordered phase or a genuinely exotic phase with non-trivial topological property, remains an unsolved question.

VI. CONCLUSIONS

We have studied the particle-hole symmetry in the KMH model, which results in the absence of the charge and spin currents and the absence of the quantum Monte-Carlo sign problem. The determinant QMC simulations have been performed for both the bulk and edge properties. The bulk antiferromagnetic long range order appears at large values of U . With the open boundary condition, the antiferromagnetic correlation is strongest along edges.

We also studied the stability of helical edges in paramagnetic insulating phase when turn on infinitesimal two-particle backscattering term, which can be introduced by time-reversal invariant but S_z not conserved interaction terms. The paramagnetic insulating phase in Fig. 3 can be classified into two regimes of weak and intermediate interactions, respectively. In the weak interaction regime, the helical edge states remain gapless which is robust against the two-particle back-scattering; in the intermediate interaction regime, the edge states can spontaneously break time-reversal symmetry by developing magnetic ordering along the edge by the two-particle backscattering term. Since this destabilizing helical edges occurs when the bulk remains time-reversal invariant, it is an interesting and open question whether the non-trivial bulk Z_2 -topology is still maintained in this regime.

We also checked that the spin-liquid phase in the Hubbard model at $\lambda = 0$ in the honeycomb lattice is neither a spontaneously developed Haldane-type quantum anomalous Hall insulator, nor, the Kane-Mele type quantum spin Hall insulator.

Acknowledgement

C. W. and D. Z. thank J. E. Hirsch for his education on the determinate quantum Monte-Carlo simulations and his encouragement on this work. C. W. is grateful to S. Kivelson for suggesting the simulation in Section V, and thanks L. Balents, L. Fu, T. Xiang for helpful discussions. C. W. is supported by ARO-W911NF0810291 and Sloan Research Foundation. D. Z. and G. M. Z. are supported by NSF of China and the National Program for Basic Research of MOST-China.

Note Added During the preparation of this

manuscript, we learned the work on the QMC simulation on the same KMH model by Hohenadler *et al* [40].

Appendix A: Absence of the sign problem for the zero temperature QMC simulations

In this appendix, we prove the absence of the sign problem of the KMH model at half-filling for zero temperature determinant QMC, which is essentially an imaginary time projector algorithm. The explanation to the algorithm can be find in Ref. [37]. For readers' convenience, we also give a brief introduction below.

The Hamiltonian composes of free and interaction parts

$$H = H_t + H_I. \quad (\text{A1})$$

The free part reads

$$H_t = \sum_{i,j} c_{i,\sigma}^\dagger K_{i,j}^\sigma c_{j,\sigma}, \quad (\text{A2})$$

where the kinetic energy matrix kernels K^\uparrow and K^\downarrow of the Kane-Mele model in Eq. A2 are given in Section II. They satisfy the relation of Eq. 11. The interaction part is

$$H_I = \frac{U}{2} \sum_i (n_{i\uparrow} + n_{i\downarrow} - 1)^2. \quad (\text{A3})$$

The expectation value of a physical observable operator \hat{O} at zero temperature is defined as

$$\langle \hat{O} \rangle = \frac{\langle \psi_0 | \hat{O} | \psi_0 \rangle}{\langle \psi_0 | \psi_0 \rangle} = \frac{\langle \psi_T | e^{-\Theta H} \hat{O} e^{-\Theta H} | \psi_T \rangle}{\langle \psi_T | e^{-2\Theta H} | \psi_T \rangle}, \quad (\text{A4})$$

where $|\psi_0\rangle$ is the ground state; Θ is a projection parameter large enough to ensure the trial wavefunction $|\psi_T\rangle$ is projected to the ground state $|\psi_0\rangle$. The discretized HS transformation of the interaction term Eq. A3 is performed in the density channel as the same as that in Eq. 9. The imaginary time propagator, i.e., the projection operator, is represented as

$$e^{-\Theta H} = \sum_{\{l\}} \left\{ U_{\{l\}}(\Theta, 0) \prod_{i,p} \gamma_{i,p}(l) e^{-i\eta_{i,p}(l)\sqrt{\Delta\tau\frac{U}{2}}} \right\},$$

$$U_{\{l\}}(\Theta, 0) = \prod_{p=M}^1 e^{-\Delta\tau \sum_{i,j} c_{i\uparrow}^\dagger K_{ij}^\uparrow c_{j\uparrow}} e^{i\sqrt{\Delta\tau\frac{U}{2}} \sum_i c_{i\uparrow}^\dagger \eta_{i,p}(l) c_{i\uparrow}}$$

$$\times \prod_{p=M}^1 e^{-\Delta\tau \sum_{i,j} c_{i\downarrow}^\dagger K_{ij}^\downarrow c_{j\downarrow}} e^{i\sqrt{\Delta\tau\frac{U}{2}} \sum_i c_{i\downarrow}^\dagger \eta_{i,p}(l) c_{i\downarrow}}, \quad (\text{A5})$$

where $\gamma_{i,p}(l)$ and $\eta_{i,p}(l)$ are the space-time discretized HS fields defined in Eq. 9 with l taking values of $\pm 1, \pm 2$; $\sum_{\{l\}}$ represents the summation over the spatial and temporal configurations of the HS field; $U_{\{l\}}(\Theta, 0)$ is the propagation operator for the HS configuration $\{l\}$.

The trial wavefunction $|\psi_T\rangle$ is required to be a Slater determinant, which we will specify later. The ground state $|\psi_0\rangle$ can be obtained from applying the imaginary time propagator $e^{-\Theta H}$ of Eq. A5 on $|\psi_T\rangle$ as

$$|\psi_0\rangle = \sum_{\{l\}} \left\{ U_{\{l\}}(\Theta, 0) \prod_{i,p} \gamma_{i,p}(l) e^{-i\eta_{i,p}(l)\sqrt{\Delta\tau\frac{U}{2}}} \right\} |\psi_T\rangle, \quad (\text{A6})$$

We further perform the calculation of Eq. A4 as

$$\langle \hat{O} \rangle = \frac{\sum_{\{l\}} \left\{ \langle \psi_T | U_l(2\Theta, \Theta) \hat{O} U_l(\Theta, 0) | \psi_T \rangle \prod_{i,p} \gamma_{i,p}(l) e^{-i\eta_{i,p}(l)\sqrt{\Delta\tau\frac{U}{2}}} \right\}}{\sum_{\{l\}} \langle \psi_T | U_l(2\Theta, 0) | \psi_T \rangle \prod_{i,p} \gamma_{i,p}(l) e^{-i\eta_{i,p}(l)\sqrt{\Delta\tau\frac{U}{2}}}} = \sum_{\{l\}} P_{\{l\}} \langle \hat{O} \rangle_{\{l\}}, \quad (\text{A7})$$

where $\langle O \rangle_{\{l\}}$ is the average value of \hat{O} for the space-time HS configuration $\{l\}$ defined as

$$\langle O \rangle_{\{l\}} = \frac{\langle \psi_T | U_{\{l\}}(2\Theta, \Theta) \hat{O} U_{\{l\}}(\Theta, 0) | \psi_T \rangle}{\langle \psi_T | U_{\{l\}}(2\Theta, 0) | \psi_T \rangle}, \quad (\text{A8})$$

and $P_{\{l\}}$ is the corresponding probability of the HS field configuration $\{l\}$ as

$$P_{\{l\}} = \frac{1}{Z} \langle \psi_T | U_l(2\Theta, 0) | \psi_T \rangle \prod_{i,p} \gamma_{i,p}(l) e^{-i\eta_{i,p}(l)\sqrt{\Delta\tau\frac{U}{2}}}. \quad (\text{A9})$$

Z is defined as $Z = \sum_{\{l\}} P_{\{l\}}$. The summation over the HS configurations $\{l\}$ can be done by using the Monte Carlo method.

Next we prove the absence of the sign problem for the KMH model with purely imaginary NNN hoppings at half-filling in the zero temperature QMC method, i.e., the probability $P_{\{l\}}$ is positive-definite. We factorize the $|\psi_T\rangle = |\psi_T^{N\uparrow}\rangle \otimes |\psi_T^{N\downarrow}\rangle$, where $|\psi_T^{N\uparrow}\rangle$ is a Slater-determinant state for spin- \uparrow electrons with the particle number N^\uparrow , and similar convention applies for $|\psi_T^{N\downarrow}\rangle$. Then $P_{\{l\}}$ reads as

$$\begin{aligned}
P_{\{l\}} &= \frac{1}{Z} \langle \psi_T^{N^\uparrow} | \prod_{p=2M}^1 e^{-\Delta\tau \sum_{i,j} c_{i\uparrow}^\dagger K_{ij}^\uparrow c_{j\uparrow}} e^{i\sqrt{\Delta\tau U/2} \sum_i \eta_{i,p}(l) (c_{i\uparrow}^\dagger c_{i\uparrow} - \frac{1}{2})} | \psi_T^{N^\uparrow} \rangle \\
&\times \langle \psi_T^{N^\downarrow} | \prod_{p=2M}^1 e^{-\Delta\tau \sum_{i,j} c_{i\downarrow}^\dagger K_{ij}^\downarrow c_{j\downarrow}} e^{i\sqrt{\Delta\tau U/2} \sum_i \eta_{i,p}(l) (c_{i\downarrow}^\dagger c_{i\downarrow} - \frac{1}{2})} | \psi_T^{N^\downarrow} \rangle \prod_{i,p} \gamma_{i,p}(l), \tag{A10}
\end{aligned}$$

where the matrices K_{ij}^\uparrow and K_{ij}^\downarrow satisfy the relation of Eq. 11; the HS fields $\gamma_{i,p}(l)$ are positive-definite.

Let us perform a particle-hole transformation only to the spin- \downarrow component

$$c_{i\downarrow}^\dagger \rightarrow d_{i\downarrow} = (-1)^i c_{i\downarrow}^\dagger, \quad c_{i\downarrow} \rightarrow d_{i\downarrow}^\dagger = (-1)^i c_{i\downarrow}, \tag{A11}$$

then Slater-determinant state $|\psi_T^{N^\downarrow}\rangle$ changes to another Slater-determinant state of holes with the hole number $N - N^\downarrow$ denoted as $|\psi_T^{h,N-N^\downarrow}\rangle$. We arrive at

$$\begin{aligned}
P_{\{l\}} &= \frac{1}{Z} \langle \psi_T^{N^\uparrow} | \prod_{p=2M}^1 e^{-\Delta\tau \sum_{i,j} c_{i\uparrow}^\dagger K_{ij}^\uparrow c_{j\uparrow}} \\
&\times e^{i\sqrt{\Delta\tau U/2} \sum_i \eta_{i,p}(l) (c_{i\uparrow}^\dagger c_{i\uparrow} - \frac{1}{2})} | \psi_T^{N^\uparrow} \rangle \\
&\times \langle \psi_T^{h,N-N^\downarrow} | \prod_{p=2M}^1 e^{-\Delta\tau \sum_{i,j} d_{i\downarrow}^\dagger K_{ij}^\downarrow d_{j\downarrow}} \\
&\times e^{-i\sqrt{\Delta\tau U/2} \sum_i \eta_{i,p}(l) (d_{i\downarrow}^\dagger d_{i\downarrow} - \frac{1}{2})} | \psi_T^{h,N-N^\downarrow} \rangle \\
&\times \prod_{i,p} \gamma_{i,p}(l). \tag{A12}
\end{aligned}$$

Now we add back the explicit form of the Slater-determinant states $|\psi_T^{N^\uparrow}\rangle$ and $|\psi_T^{h,N-N^\downarrow}\rangle$ as

$$\begin{aligned}
|\psi_T^{N^\uparrow}\rangle &= \prod_{j=1}^{N^\uparrow} \left(\sum_{i=1}^N c_i^\dagger Q_{ij}^\uparrow \right) |0\rangle = \prod_{j=1}^{N^\uparrow} \left(\vec{c}^\dagger Q^\uparrow \right)_j |0\rangle, \\
|\psi_T^{h,N-N^\downarrow}\rangle &= \prod_{j=1}^{N-N^\downarrow} \left(\sum_{i=1}^N d_i^\dagger Q_{ij}^\downarrow \right) |0\rangle_h \\
&= \prod_{j=1}^{N-N^\downarrow} \left(\vec{d}^\dagger Q^\downarrow \right)_j |0\rangle_h, \tag{A13}
\end{aligned}$$

where $|0\rangle$ and $|0\rangle_h$ are the particle vacuum and hole vacuum states, respectively; N is the number of lattice sites; Q^\uparrow is a $N \times N^\uparrow$ -dimensional rectangular matrix, and Q^\downarrow is a $N \times (N - N^\downarrow)$ -dimensional matrix; \vec{c}^\dagger and \vec{d}^\dagger are vector notations for c_i^\dagger and d_i^\dagger with $i = 1$ to N .

The Slater-determinant wavefunction has nice properties as

$$e^{\vec{c}^\dagger M \vec{c}} \prod_{j=1}^{N_p} (\vec{c}^\dagger Q)_j |0\rangle = \prod_{j=1}^{N_p} [\vec{c}^\dagger e^M Q^\uparrow]_j |0\rangle, \tag{A14}$$

and

$$\begin{aligned}
&\langle 0 | \prod_{j=1}^{N_p} (\vec{c} Q^\dagger)_j e^{\vec{c}^\dagger M \vec{c}} \prod_{j=1}^{N_p} (\vec{c}^\dagger Q')_j |0\rangle \\
&= \det [Q^\dagger e^M Q'], \tag{A15}
\end{aligned}$$

where M is an $N \times N$ Hermitian matrix, or anti-Hermitian matrix. Based on these properties, we have

$$\begin{aligned}
P_{\{l\}} &= \det \left[(Q^\uparrow)^\dagger \left(\prod_{p=2M}^1 e^{-K^\uparrow} e^{iV_p(l)} \right) Q^\uparrow \right] \\
&\times \det \left[(Q^\downarrow)^\dagger \left(\prod_{p=2M}^1 e^{-K^\downarrow} e^{-iV_p(l)} \right) Q^\downarrow \right] \\
&\times \prod_{i,p} \gamma_{i,p}(l), \tag{A16}
\end{aligned}$$

where the matrix kernels satisfy $K^\uparrow = (K^\downarrow)^*$ and $V_p(l)$ is a purely real diagonal matrix whose i -th diagonal element reads

$$[V_p(l)]_{ii} = \sqrt{\Delta\tau \frac{U}{2}} \eta_{i,p}(l). \tag{A17}$$

If we set the trial wavefunction to satisfy $N^\uparrow = N^\downarrow = N/2$ and $Q^\downarrow = (Q^\uparrow)^*$, then we have

$$\begin{aligned}
P_{\{l\}} &= \frac{1}{Z} \left| \det \left[(Q^\uparrow)^\dagger \left(\prod_{p=2M}^1 e^{-K^\uparrow} e^{V_p(l)} \right) Q^\uparrow \right] \right|^2 \\
&\times \prod_{i,p} \gamma_{i,p}(l), \tag{A18}
\end{aligned}$$

thus the probability distribution $P_{\{l\}}$ is positive-definite at half-filling.

-
- [1] D. J. Thouless, M. Kohmoto, M. P. Nightingale, and M. den Nijs, *Phys. Rev. Lett.* **49**, 405 (1982).
- [2] M. Kohmoto, *Ann. Phys.* **160**, 296 (1985).
- [3] X. Qi and S. Zhang, arXiv:1008.2026 (2010).
- [4] M. Z. Hasan and C. L. Kane, *Rev. Mod. Phys.* **82**, 3045 (2010).
- [5] B. A. Bernevig, T. L. Hughes, and S.-C. Zhang, *Science* **314**, 1757 (2006).
- [6] X.-L. Qi, T. L. Hughes, and S.-C. Zhang, *Phys. Rev. B* **78**, 195424 (2008).
- [7] C. L. Kane and E. J. Mele, *Phys. Rev. Lett.* **95**, 146802 (2005).
- [8] D. N. Sheng, Z. Y. Weng, L. Sheng, and F. D. M. Haldane, *Phys. Rev. Lett.* **97**, 036808 (2006).
- [9] J. E. Moore and L. Balents, *Phys. Rev. B* **75**, 121306 (2007).
- [10] R. Roy, *Phys. Rev. B* **79**, 195321 (2009).
- [11] L. Fu, C. L. Kane, and E. J. Mele, *Phys. Rev. Lett.* **98**, 106803 (2007).
- [12] L. Fu and C. L. Kane, *Phys. Rev. B* **76**, 045302 (2007).
- [13] H. Zhang, C.-X. Liu, X.-L. Qi, X. Dai, Z. Fang, and S.-C. Zhang, *Nat Phys* **5**, 438 (2009).
- [14] C. Wu, B. A. Bernevig, and S.-C. Zhang, *Phys. Rev. Lett.* **96**, 106401 (2006).
- [15] C. Xu and J. E. Moore, *Phys. Rev. B* **73**, 064417 (2006).
- [16] M. König, S. Wiedmann, C. Brüne, A. Roth, H. Buhmann, L. W. Molenkamp, X. L. Qi, and S. C. Zhang, *Science* **318**, 766 (2007).
- [17] D. Hsieh, D. Qian, L. Wray, Y. Xia, Y. S. Hor, R. J. Cava, and M. Z. Hasan, *Nature* **452**, 970 (2008).
- [18] D. Hsieh, Y. Xia, L. Wray, D. Qian, A. Pal, J. H. Dil, J. Osterwalder, F. Meier, G. Bihlmayer, C. L. Kane, Y. S. Hor, R. J. Cava, and M. Z. Hasan, *Science* **323**, 919 (2009).
- [19] Y. Xia, D. Qian, D. Hsieh, L. Wray, A. Pal, H. Lin, A. Bansil, D. Grauer, Y. S. Hor, R. J. Cava, and M. Z. Hasan, *Nat Phys* **5**, 398 (2009).
- [20] Y. L. Chen, J. G. Analytis, J.-H. Chu, Z. K. Liu, S.-K. Mo, X. L. Qi, H. J. Zhang, D. H. Lu, X. Dai, Z. Fang, S. C. Zhang, I. R. Fisher, Z. Hussain, and Z.-X. Shen, *Science* **325**, 178 (2009).
- [21] P. Roushan, J. Seo, C. V. Parker, Y. S. Hor, D. Hsieh, D. Qian, A. Richardella, M. Z. Hasan, R. J. Cava, and A. Yazdani, *Nature* **460**, 1106 (2009).
- [22] Z. Alpichshev, J. G. Analytis, J.-H. Chu, I. R. Fisher, Y. L. Chen, Z. X. Shen, A. Fang, and A. Kapitulnik, *Phys. Rev. Lett.* **104**, 016401 (2010).
- [23] T. Zhang, P. Cheng, X. Chen, J.-F. Jia, X. Ma, K. He, L. Wang, H. Zhang, X. Dai, Z. Fang, X. Xie, and Q.-K. Xue, *Phys. Rev. Lett.* **103**, 266803 (2009).
- [24] Z. Cai, S. Chen, S. Kou, and Y. Wang, *Phys. Rev. B* **78**, 035123 (2008).
- [25] S. Rachel and K. Le Hur, *Phys. Rev. B* **82**, 075106 (2010).
- [26] S. Raghu, X.-L. Qi, C. Honerkamp, and S.-C. Zhang, *Phys. Rev. Lett.* **100**, 156401 (2008).
- [27] K. Sun, H. Yao, E. Fradkin, and S. A. Kivelson, *Phys. Rev. Lett.* **103**, 046811 (2009).
- [28] Y. Zhang, Y. Ran, and A. Vishwanath, *Phys. Rev. B* **79**, 245331 (2009).
- [29] J. Wen, A. Rugg, C. C. Joseph Wang, and G. A. Fiete, *Phys. Rev. B* **82**, 075125 (2010).
- [30] C. N. Varney, K. Sun, M. Rigol, and V. Galitski, *Phys. Rev. B* **82**, 115125 (2010).
- [31] R. Blankenbecler, D. J. Scalapino, and R. L. Sugar, *Phys. Rev. D* **24**, 2278 (1981).
- [32] J. E. Hirsch, *Phys. Rev. B* **31**, 4403 (1985).
- [33] S. Chandrasekharan and U.-J. Wiese, *Phys. Rev. Lett.* **83**, 3116 (1999).
- [34] S. E. Koonin, D. J. Dean, and K. Langanke, *Phys. Rep.* **278**, 1 (1997).
- [35] C. Wu and S.-C. Zhang, *Phys. Rev. B* **71**, 155115 (2005).
- [36] Z. Y. Meng, T. C. Lang, S. Wessel, F. F. Assaad, and A. Muramatsu, *Nature (London)* **464**, 847 (2010).
- [37] F. F. Assaad and H. G. Evertz, *Lect. Notes. Phys.* **739**, 277 (2008).
- [38] H. Feldner, Z. Y. Meng, T. C. Lang, F. F. Assaad, S. Wessel, and A. Honecker, *Phys. Rev. Lett.* **106**, 226401 (2011).
- [39] S. Kivelson, private communication.
- [40] M. Hohenadler, T. C. Lang, and F. F. Assaad, *Phys. Rev. Lett.* **106**, 100403 (2011).